

TECHNIQUES FOR ASSESSING SPACE OBJECT CATALOGUING PERFORMANCE DURING DESIGN OF SURVEILLANCE SYSTEMS

Jan Siminski*

ESA/ESOC Space Debris Office
Robert-Bosch-Straße 5, 64293 Darmstadt, Germany
jan.siminski@esa.int

ABSTRACT

In order to guarantee safe operation of satellites, space object catalogues must be build-up and maintained. The catalogues should be complete, i.e. contain sufficiently accurate and frequently updated orbital states for all required objects.

In theory, completeness of the catalogue is achieved by designing the radar in a way that a major fraction of the object population is considered detectable, i.e. covered by the sensor's field-of-regard and within the sensor sensitivity. However, complete coverage does not necessarily guarantee a proper catalogue build-up, yet. If an object is observed once, it must be re-observed in order to verify its existence and improve the accuracy of the determined state. In a next step, individual observation tracks are combined with each other to further improve the accuracy. Consequently, tracks must be associated to each other, i.e. tested if they originate from the same object or not.

The success rate of the association is dependent on the quality of the tracks, the re-observation time and the re-observation geometry. For surveillance radars, the association performance must be considered as a critical design parameter and can be optimized along with the detection rate during the design process. We outline the underlying techniques and present a simulation-based framework for assessing the surveillance system design in terms of association performance and achievable accuracy.

Index Terms— track association, radar design, space debris, orbit determination, orbit accuracy

1. INTRODUCTION

In order to assess the cataloguing capabilities of a radar sensor, all individual steps of the cataloguing process must be tested. The developed toolbox consists of several independent functions, each one performing one cataloguing task. The structure of the paper resembles the structure of the toolbox, i.e. each function required for a step is outlined in one section

and the order of the sections follows the typical processing order. The individual steps are:

1. Simulation of the sensor and object population
2. Initial orbit determination with single radar tracks
3. Association of two radar tracks
4. Orbit accuracy using a consider covariance analysis.

Phased-array radars are defined with a detection figure-of-merit (i.e. ratio of detectable object size at a certain distance), a field-of-view, a pointing direction, and a noise estimate. Then, observations are generated with a realistic object population model. The resulting tracks are associated to each other using covariance-based distance metrics. We address several difficulties which arise during the association, e.g. proper treatment of state uncertainties and robust initial orbit determination. The association performance is finally analysed for different orbital heights and re-observation conditions. Additionally, the typical resulting orbital state accuracies are presented for the initial orbits as well as for the improved ones. All steps and functions are mathematically described and accompanied with an example analysis for a test radar located in central Europe.

2. OBSERVATIONS / SIMULATION

The reference object population is taken from ESA's MASTER model. Each object is described by orbital elements, a diameter d and an area-to-mass ratio. The latter is used to define a ballistic coefficient B by randomly assigning drag coefficients. In order to speed up computations in the early stages of the design phase, the propagation of object states is implemented using the analytical SGP4 theory.

The simulated phased-array radars repeatedly scan a wide field-of-view (with small revisit times, e.g. a few seconds). Whenever an object passes the field and is detectable, the sensor estimates a series of range values ρ and line-of-sight vectors \mathbf{u} (usually described by deflection angles α and β , or alternatively azimuth and elevation).

A simplified detection model decides if an object is visible using the relative radar range equation, i.e. the radar performance is described in terms of a minimum object diame-

*Funded by the national trainee programme of the German Aerospace Center (DLR).

ter d_{\min} visible at a reference distance ρ_{ref} assuring a certain signal-to-noise ratio (SNR_{\min})

$$\frac{d^2}{\rho^4} \geq \frac{d_{\min}^2}{\rho_{\text{ref}}^4} \propto \text{SNR}_{\min}. \quad (1)$$

The diameter describes the reflection area in this equation. This assumption, however, is only valid if the object size is above a certain threshold depending on the used frequency band. The radar cross-section decreases more rapidly if the object size is within the so-called Rayleigh region of the band. A constant cut-off diameter is therefore introduced as suggested in [1]. The detection test is performed for each object crossing the field-of-regard. In order to reduce computation time, the overall population is filtered beforehand using the perigee altitude as the smallest possible range (cf. with the approach in [1]).

The observation noise is accounted in the simulation by adding SNR-dependent random errors to the measured angles and ranges. The standard deviation of range σ_ρ and angles $\sigma_{\alpha,\beta}$ are described with the proportional relation

$$\sigma_\rho^2 \propto \frac{1}{\text{SNR}} \quad \text{and} \quad \sigma_{\alpha,\beta}^2 \propto \frac{1}{\text{SNR}}. \quad (2)$$

The signal-to-noise ratio for each detection is computed by scaling the minimum signal-to-noise ratio in (1) according to the current distance and diameter. Consequently, when providing a maximum standard deviation for the observables, they are equally scaled for each observation. Instead of scaling the maximum deviation, radar design parameters can be specified, such as range resolution and beam-width (cf. [2]).

2.1. Example setup

An example radar setup is used throughout this paper to visualize and validate the functionality of the different steps in the simulation. For simplicity, a single phased-array radar is simulated, however, the toolbox can be extended to support a sensor network design. The above described performance parameters for the sensor are shown in Table 1.

Table 1. Example radar setup

Parameter	ρ_{ref}	d_{\min}	$\sigma_{\rho,\text{max}}$	$\sigma_{\alpha,\beta,\text{max}}$
Value	1000 km	10 cm	5 m	0.2°

The radar is south-pointing with 60° elevation and a $100^\circ \times 30^\circ$ field-of-view (defined in deflection angles). The revisit time is assumed to be 10 seconds.

The simulated population for this parameters is shown in Figure 1. In order to emphasize the signal-to-noise detection boundary (dashed line), the illustration is cut-off to show only small objects (≤ 30 cm). Around 19,000 objects are theoretically visible for the radar and simulated for a period of 14

days. Highly populated regions appear darker in the illustration. The orbit determination and association steps are presented and discussed for the here shown perigee height range between 400 and 1200 km.

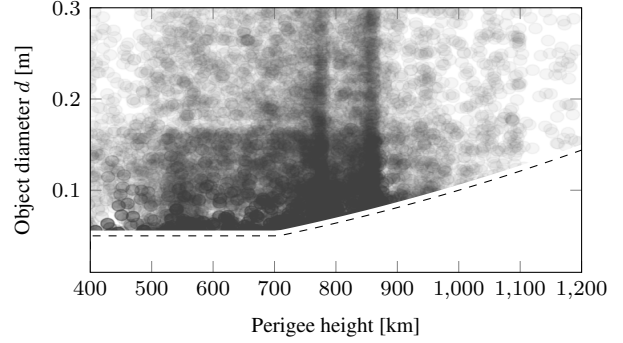


Fig. 1. Simulated objects are shown w.r.t. perigee height and diameter. The SNR detection threshold is illustrated with the dashed line. Sensor setup and details are provided in the text.

3. INITIAL ORBIT DETERMINATION

The series of n range (ρ_k) and angular measurements (α_k, β_k) at t_k for $k = 1, \dots, n$ is denoted as a track. In order to determine the state vector $\mathbf{y} = (\mathbf{r}^\top, \dot{\mathbf{r}}^\top)^\top$ describing these measurements, they are first converted into the geocentric space-fixed reference frame

$$\mathbf{r}_k = \mathbf{R}_k + \rho_k \mathbf{u}(\alpha_k, \beta_k) \quad (3)$$

using the inertial radar position \mathbf{R}_k at each epoch. The uncertainty of \mathbf{r}_k is described in terms of a multivariate normal distribution, where the covariance $\mathbf{C}_{r,k}$ is calculated by a linear transformation of the measurement uncertainty.

Several methods exist to obtain a preliminary orbit from two or three geocentric positions (e.g. Lambert's problem solver or the Herrick-Gibbs approach as provided in [3]). The GTDS Range and angles method from [4, pp. 9-44 – 9-52] provides a stable fixed-point iteration scheme using the full information of the track, i.e. all n available observations.

The developed method has been adapted from the reference, and is also able to provide the covariance. Starting from a preliminary state $\mathbf{y}^{(0)}$ (using e.g. a circular assumption or above mentioned approaches for three observations), it is iteratively updated by matrix multiplication

$$\mathbf{y}^{(i+1)} = \mathbf{H}(\mathbf{y}^{(i)}) \mathbf{z}, \quad (4)$$

where the radar observations are $\mathbf{z} = (\mathbf{r}_1^\top, \mathbf{r}_2^\top, \dots, \mathbf{r}_n^\top)^\top$ and the matrix \mathbf{H} is assembled from the series expansion about the current state estimate $\mathbf{y}^{(i)}$. The (i) denotes the i^{th} iteration of the fixed-point update process. In the series expansion, each measurement is written in terms of $\mathbf{r}_k = f_k \mathbf{r}^{(i)} + g_k \dot{\mathbf{r}}^{(i)}$.

Derivations for the f and g coefficients are provided in e.g. [3]. The set of equations is then solved for $\mathbf{r}^{(i)}$ and $\dot{\mathbf{r}}^{(i)}$. Defining $\mathbf{f} = (f_1, \dots, f_n)^\top$ and $\mathbf{g} = (g_1, \dots, g_n)^\top$, the update matrix is given by

$$\mathbf{H} = \frac{1}{\delta} \begin{pmatrix} \mathbf{g}^\top \mathbf{g} \mathbf{F} - \mathbf{f}^\top \mathbf{g} \mathbf{G} \\ \mathbf{f}^\top \mathbf{f} \mathbf{G} - \mathbf{f}^\top \mathbf{g} \mathbf{F} \end{pmatrix} \quad (5)$$

where

$$\delta = \mathbf{f}^\top \mathbf{f} \cdot \mathbf{g}^\top \mathbf{g} - (\mathbf{f}^\top \mathbf{g})^2 \quad (6)$$

is the denominator and the auxiliary matrix \mathbf{F} (and equivalently also \mathbf{G}) is defined as

$$\mathbf{F} = \begin{pmatrix} f_1 & 0 & 0 & \dots & f_n & 0 & 0 \\ 0 & f_1 & 0 & \dots & 0 & f_n & 0 \\ 0 & 0 & f_1 & \dots & 0 & 0 & f_n \end{pmatrix}. \quad (7)$$

The method converges towards the solution \mathbf{y} . The covariance of the state is determined by transforming all individual measurement covariances $\mathbf{C}_{r,k}$ using the linear approximation

$$\mathbf{C}_y = \mathbf{H} \mathbf{C}_z \mathbf{H}^\top, \text{ where } \mathbf{C}_z = \text{diag}(\mathbf{C}_{r,1}, \dots, \mathbf{C}_{r,n}). \quad (8)$$

Alternatively, least-squares methods can be used to improve the state. However, due to the short length of the tracks (usually a few percent of the orbit) the preliminary states, e.g. from Herrick-Gibbs, provide poor orbital estimates and undamped differential correction steps can lead to divergence of the orbit improvement. Hence, trust-region approaches must be used to ensure convergence. The presented fixed-point method showed best convergence in comparison with other implemented trust-region approaches for different tested orbital regimes and geometries.

3.1. Initial orbit accuracy

As written above, the population is propagated for 14 days, which generates around $\sim 15,000$ tracks. Each track is processed using the presented initial orbit determination method. The resulting state is compared with the simulated truth in order to assess the orbit error. The positional errors are mostly determined by the radar performance parameters, while the velocity errors are largely dependent on the track length. The analysis here focuses on the semi-major axis error, which comprise positional and velocity errors.

The mean semi-major axis error is shown in Figure 2 for different orbital heights and for the covered orbital angle $\Delta\nu$ (effectively the difference in true anomaly of first and last measurement of the track). Objects in lower altitudes typically appear for shorter durations in the field-of-regard, leading to less observations per pass, while higher objects are captured multiple times by the scanning pattern. This explains the large perigee height dependency on the upper part of the figure. A large effect on the accuracy is also observed for the orbital coverage. The longer the arc covered, the better the estimate. The orientation of the radar and the design of the field-of-regard should account for this dependency.

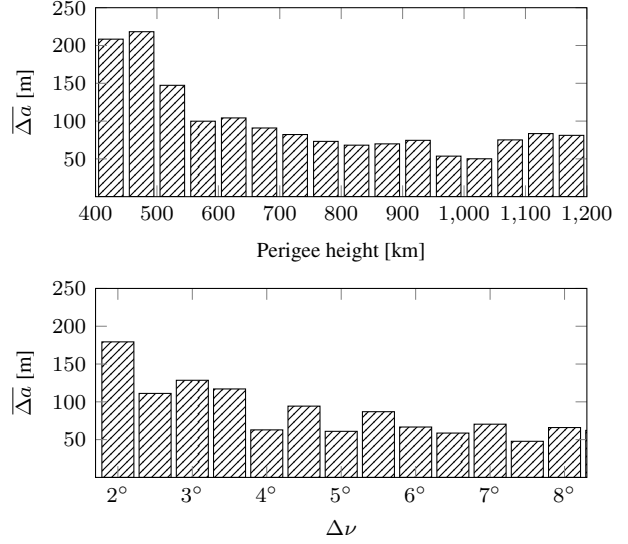


Fig. 2. Mean semi-major axis error $\overline{\Delta a}$ of initial orbit determination result depending on covered orbital arc $\Delta\nu$ and perigee height.

4. ASSOCIATION

In order to assess the association performance, all consecutive tracks of each object are tested against each other. The association test is successful if it find out that both originate from the same object. The toolbox uses the so-called covariance-based association scheme (cf. [5]). The process is shortly described in the following.

The information of two tracks is compressed in two state vectors \mathbf{y}_1 and \mathbf{y}_2 along with their uncertainties represented by \mathbf{C}_{y_1} and \mathbf{C}_{y_2} . In order to compare the two states, they are propagated to a common epoch, e.g. the first state is propagated to the observation epoch of the latter track. The modelled state is then given by $\tilde{\mathbf{y}}_2(\mathbf{y}_1)$ along with the propagated covariance $\mathbf{C}_{\tilde{\mathbf{y}}_2}(\mathbf{y}_1, \mathbf{C}_{y_1})$. The propagation of the covariance matrices is performed either using a linear approximation or other non-linear transformations (e.g. using sigma-points).

If the two normally distributed quantities are subtracted, giving $\Delta\mathbf{y} = \mathbf{y}_2 - \tilde{\mathbf{y}}_2(\mathbf{y}_1)$, the result is also normally distributed according to

$$\Delta\mathbf{y} \sim \mathcal{N}(\Delta\mathbf{y}; \mathbf{0}, \mathbf{C}_{\Delta\mathbf{y}}) \quad \text{where} \quad \mathbf{C}_{\Delta\mathbf{y}} = \mathbf{C}_{y_2} + \mathbf{C}_{\tilde{\mathbf{y}}_2}. \quad (9)$$

The exponent of the normal distribution is used as a statistical distance between the two tracks

$$L = \Delta\mathbf{y}^\top \mathbf{C}_{\Delta\mathbf{y}}^{-1} \Delta\mathbf{y} \sim \chi^2(6). \quad (10)$$

If the two tracks belong to the same object, the distance L is below a certain threshold. The threshold can be defined considering that L is chi-square distributed, i.e. it can be defined to cover a certain percentage of the chi-square distribution

(e.g. 95%). A threshold can also be calibrated to reduce the number of false associations. The latter is neglected in this paper, as the number of falsely associated observations is small for the used population and radar setup (cf. also with the analysis in [6]). However, with increasing capabilities of radars, false associations can dramatically increase the computational burden of the cataloguing software and thus become a critical design-factor as well.

The states can be represented in any coordinate system for the comparison, e.g. orbital elements or cartesian (as used for the initial orbit of the previous section). The different systems come with certain advantages and disadvantages regarding covariance realism [6]. If a satellite state with a large semi-major axis uncertainty is propagated, the error ellipsoid in cartesian space deforms rapidly into a curved shape due to the linear increase in mean anomaly uncertainty. Other effects, such as atmospheric drag, increase the deformation of covariance. Curvilinear coordinates as described by [5] consistently show better performance than cartesian. The coordinates are defined around a reference state (e.g. the state \mathbf{y}_2) and are composed of an along-track arc-length error, a cross-track arc-length and in-radial difference. A detailed derivation is given in [7]. Orbital elements show a similar performance, but the satellite-centred frame allows a better separation of position and velocity, which helps visualizing and interpreting distances.

Figure 3 shows the transformed probability density function of a satellite in low-earth orbit (semi-major axis $a = 8000$ km and eccentricity $e = 0.1$) in cartesian and curvilinear space. The initial uncertainty is normally distributed with a dominant uncertainty in the along-track velocity $\sigma_T = 0.005$ m/s (standard deviation). The state is propagated from the apogee to the perigee for 2.5 orbital periods in order to increase the deformation effect. The figure shows the deformation in cartesian space (a), while the density remains normal in curvilinear space (b).

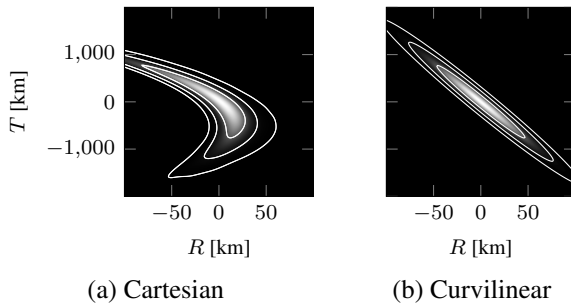


Fig. 3. Transformed probability density of a propagated satellite state (details in text) in satellite-centred coordinates (T is the tangential direction and R the in-radial one). The white lines denote contours of equal density equivalent to the $1-3\sigma$ boundaries used for the univariate normal distribution.

Instead of using an appropriate coordinate system, other

uncertainty representations such as Gaussian-mixtures can be used to overcome the deformation issue. A transformation using an adaptive Gaussian-mixture scheme, similar to [8], has been implemented to evaluate the validity of the simpler covariance based association in curvilinear space. Figure 3(a) is generated using a 500 component automatically splitted Gaussian-mixture distribution. For this type of a radar setup assessment, the simpler and computationally less expensive implementation using the beneficial coordinates is selected. Nevertheless, for real implementations and especially when tracks are separated by larger time-spans, other measures can become feasible.

4.1. Association performance

The simulated measurement set is analysed using the above mentioned covariance-based approach. The association test should, in principle, be symmetric assuming proper representation and proper transformation of uncertainties. In practice, the approximate transformation of state uncertainty introduces errors which differ from one propagated state to another (e.g. depending on initial uncertainty and geometry). Hence, each pair is tested twice, i.e. once in each direction. The smaller value of both comparisons is tested against a threshold covering 95 % of the theoretical distribution.

The resulting success rate is shown in Figure 4. The rate shows the performance for objects which have been observed at least twice within the 14 days. The performance is similar for all orbital regions, but depends largely on other quantities, namely re-observation time and track length. The upper figure shows the relation to the re-observation time, i.e. the time difference between the first and second tested track. The performance degrades over time, but promises around 90 % of successful associations for re-observations within the first day. The figure must be carefully interpreted as the individual bins contain different numbers of pairs, e.g. most objects are re-observed after 0.25–0.75 days, while a few percent is seen again only after 2 days. If the field-of-regard is wide enough to guarantee re-observations within one day, the association is mostly successful for the example radar setup.

The lower plot in Figure 4 shows the dependency of the association success on the track length. The larger orbital angle of both tracks, i.e. $\max(\Delta\nu_1, \Delta\nu_2)$, is used to compute the bin rate. The success rate degrades for smaller angles. If the information contained in a track is insufficient for finding an accurate enough preliminary orbit, other ways to associate the tracks must be found. The problem can be circumvented by determining the orbit using two tracks at a time. The combination of two short tracks using a Lambert’s problem solver for perturbed orbital motion is a topic of ongoing research (e.g. [9]). More advanced algorithms will be developed, tested, and assessed with the current simulation framework.

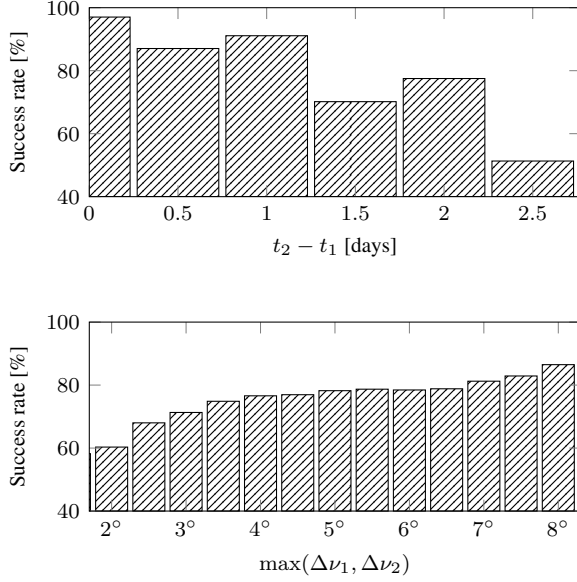


Fig. 4. Association performance for simulated observations depending on re-observation time and track length.

5. ORBIT DETERMINATION

All measurements of an object are combined to find the best possible orbital solution. In the simulated example, around 10 – 50 tracks are collected for the objects depending on the repeatability of the ground-track. Instead of selecting a fixed fit span (e.g. 14 days) for all objects, each one gets one assigned according to the object parameters and orbit type.

More measurements typically improve the estimate of an orbit, however, unmodelled or insufficiently modelled dynamics cause the fit to degrade after some time. Thus, the optimal fit span is constrained by the model insufficiencies, mostly caused by the approximately known densities in the atmosphere. The effect of the atmosphere on an orbit can be described in terms of the energy dissipation rate \dot{E}_D as described in [10]. In order to speed up computations, analytical formulas to approximate it, derived by [11], are used.

So far, the optimal fit span is determined by using a simple linear relation to the logarithm of \dot{E}_D and additionally upper and lower bounds. The function is calibrated with typical values from experience (i.e. fit spans covering a few days up to 2 weeks). However, other more elaborate functions can be implemented, which take individual orbital classes into account.

5.1. Consider covariance analysis

The achievable orbit accuracy of the tested radar setup is assessed using a consider covariance analysis. The method is described in various textbooks about orbit determination (such as [12] and [13]).

When determining the orbit of a satellite, some param-

eters \mathbf{x} are estimated (solved-for parameters such as the orbital elements and the ballistic coefficient) and some model parameters are fixed because they are unknown (e.g. atmospheric density variations, bias terms, or satellite attitude). The latter simplifications, however, introduce errors which have to be accounted. Hence, the values are introduced as consider parameters \mathbf{c} into the covariance calculation with their uncertainty represented by the covariance \mathbf{C}_c . The covariance accounting only for measurement noise, represented by the weighting matrix \mathbf{W} , is calculated with

$$\mathbf{C}_x = (\mathbf{H}_x^T \mathbf{W} \mathbf{H}_x)^{-1} \quad (11)$$

and the covariance accounting for the uncertain consider parameters \mathbf{c} is then given by

$$\mathbf{C}_x^c = \mathbf{C}_x + (\mathbf{C}_x \mathbf{H}_x^T \mathbf{W}) (\mathbf{H}_c \mathbf{C}_c \mathbf{H}_c) (\mathbf{C}_x \mathbf{H}_x^T \mathbf{W})^T, \quad (12)$$

where the partials of the function \mathbf{h} , modelling the observations from the state, are given by

$$\mathbf{H}_x = \frac{\partial \mathbf{h}}{\partial \mathbf{x}} \quad \text{and} \quad \mathbf{H}_z = \frac{\partial \mathbf{h}}{\partial \mathbf{z}} \quad (13)$$

and are evaluated at the known solution of the inversion problem.

Error sources such as a range bias are reduced by proper calibration of the system. They can often only be estimated when combining measurements from other sensors. The dominant error source for satellites in low-earth orbits is the atmospheric drag \mathbf{a}_D . Due to the complexity of the system, accurate models are difficult to generate. When tracking unknown objects, the object properties and attitude is unknown and possibly constantly changing. Typically, one average or multiple piecewise-defined ballistic coefficients B are estimated which absorb some effects (alternatively so-called pseudo-accelerations are used). Some random variations, however, cannot be captured by this average value. That is why, analogously to the approach presented in [14], the drag acceleration term is augmented with a correction factor

$$\mathbf{a}_D^c = \mathbf{a}_D(B, \mathbf{y}, t)(1 + w(t)). \quad (14)$$

The factor w models the variation and thus changes with time. For simplicity, the function is assumed to be constant for equally spaced time intervals τ_w , where w_i is the value for each interval. The covariance \mathbf{C}_c is then assembled from

$$\mathbb{E}[w_i] = 0 \quad \text{and} \quad \mathbb{E}[w_i w_j] = \sigma_w^2 \exp\{-|i - j| \tau_w\}. \quad (15)$$

The noise is modelled as a correlated random walk (stochastic process) in accordance with [14]. Instead of using one interval τ_w (e.g. once per day), the accumulation of different effects can be included by adding up multiple factors, each with another interval (e.g. once per day, once per orbital revolution, and once per hour variation).

An illustration of such a random walk is shown in Figure 5. Each dot illustrates one interval (or step) of the walk. The estimated ballistic coefficient B (dashed) is used to illustrate the $w = 0$ line.

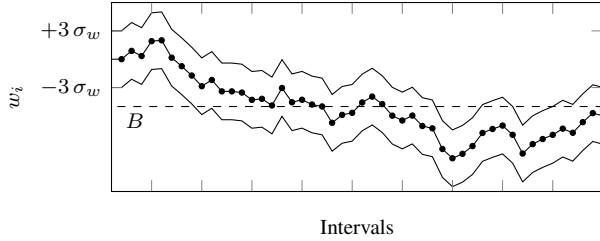


Fig. 5. Illustration of the Gaussian random walk. The dots denote deviation for each step from the estimated B , and solid lines denote the $3\sigma_w$ boundary. The dashed line illustrates the mean B over the whole orbit determination interval.

5.2. Catalog accuracy

This section shows the preliminary results of the achievable catalogue accuracy. Only the drag uncertainty is included in this analysis (with $\sigma_w = 5\%$ and an one day interval) as other effects are hidden behind the large effect of it. The used values must be compared and calibrated with values and experiences from real orbit determination results before continuing the analysis.

Figure 6 shows the results for different orbital heights (represented with perigee height). The accuracy is illustrated with the median standard deviation σ for position (upper plot) and velocity (lower plot) in the satellite-centered radial, along-track, and cross-track reference frame. The median is selected over the mean as multiple outliers with very large uncertainties distort the latter quantity. The figure thus shows that 50% of the simulated objects have better accuracies than the indicated values. For instance, the highly populated region with a perigee height around 800 km is mostly determined with an uncertainty of around 100 m in the along-track component and around 0.01 m/s uncertainty in the respective velocity component.

6. SUMMARY AND CONCLUSION

The paper presents a tool developed to assess sensor capabilities in terms of cataloguing performance. The simulation of sensor and population is performed using simplified assumptions on observation conditions. In the framework of the analysis, a toolbox of initial orbit determination methods and association measures has been developed. Additional methods which allow the association of very short radar tracks are currently in development. The methods to test the achievable accuracy of a catalogue can be used to compare different designs. However, in order to provide realistic absolute numbers, it must be calibrated using real data. This also includes a realistic estimation of orbit determination fit spans (using e.g. several orbital classes depending on the energy dissipation rate).

The presented results are always shown in terms of the

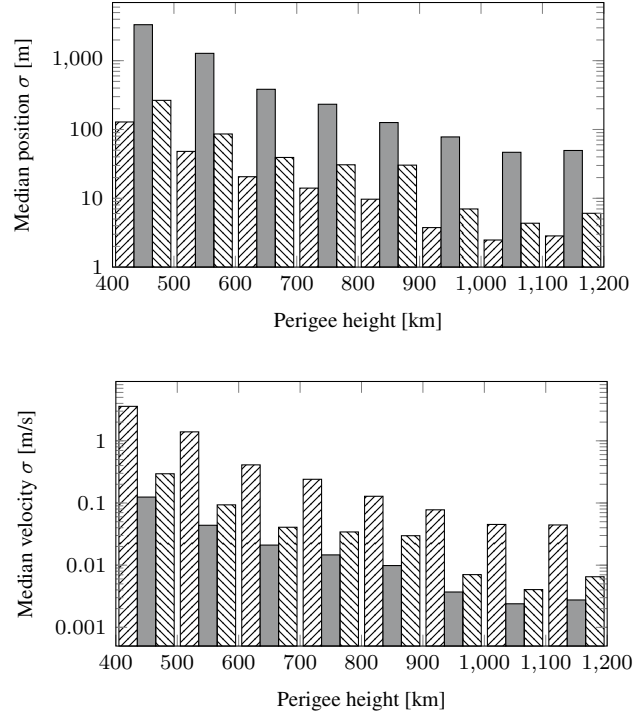


Fig. 6. Median standard deviation in radial (///), along-track (■), and cross-track (▩) frame dependent on perigee height.

successfully observed population and not the overall simulated one. In order to quantify the success for the whole population, more realistic observation models must be implemented. Other tools, such as PROOF [15], focus on realistic observation and detection modelling (with detailed analyses) and can be incorporated into the analysis.

So far, the tools are able to assess a sensor design, e.g. to evaluate and compare industry offers. The next step is to use it for the design of a sensor or sensor network, e.g. by analysing the influence of key sensor parameters such as location, field-of-regard, pointing, performance parameters, and other properties.

7. REFERENCES

- [1] H. Krag, H. Klinkrad, T. Flohrer, and E. Fletcher, “Service design drivers and solution concepts for a European LEO space surveillance system,” in *61st International Astronautical Congress*, Prague, Czech Republic, September 2010, International Astronautical Federation.
- [2] G.R. Curry, *Radar System Performance Modeling*, Artech House, Boston, 2nd edition, 2005.
- [3] D.A. Vallado and W.D. McClain, *Fundamentals of astrodynamics and applications*, Microcosm Press,

- Hawthorne / Springer-Verlag, New York, 3rd edition, 2007.
- [4] A.C. Long, J.O. Cappellari Jr, C.E. Velez, and A.J. Fuchs, "Goddard trajectory determination system (GTDS) mathematical theory (revision 1)," Tech. Rep. FDD/552-89/001 and CSC/TR-89/6001, National Aeronautics and Space Administration/Goddard Space Flight Center, July 1989.
- [5] K. Hill, K. Alfriend, and C. Sabol, "Covariance-based uncorrelated track association," in *AIAA/AAS Astrodynamics Specialist Conference and Exhibit*, Honolulu, Hawaii, USA, August 2008, American Institute of Aeronautics and Astronautics.
- [6] K. Hill, C. Sabol, and K. Alfriend, "Comparison of covariance-based track association approaches using simulated radar data," *The Journal of the Astronautical Sciences*, vol. 59, no. 1-2, pp. 281–300, 2012.
- [7] D. A. Vallado and S. Alfano, "Curvilinear coordinate transformations for relative motion," *Celestial Mechanics and Dynamical Astronomy*, vol. 118, no. 3, pp. 253–271, 2014.
- [8] K. J. DeMars, R. H. Bishop, and M. K. Jah, "Entropy-based approach for uncertainty propagation of nonlinear dynamical systems," *Journal of Guidance, Control, and Dynamics*, vol. 36, no. 4, pp. 1047–1057, 2013.
- [9] G. F. Gronchi, L. Dimare, D. Bracali Cioci, and H. Ma, "On the computation of preliminary orbits for earth satellites with radar observations," *Monthly Notices of the Royal Astronomical Society*, vol. 451, no. 2, pp. 1883–1891, 2015.
- [10] J.G. Miller, "A new sensor allocation algorithm for the space surveillance network," *Military Operations Research*, vol. 12, no. 1, pp. 57–70, 2007.
- [11] D.G. King-Hele, *Satellite orbits in an atmosphere: theory and application*, Springer Science & Business Media, 1987.
- [12] O. Montenbruck and E. Gill, *Satellite orbits: models, methods and applications*, Springer-Verlag Berlin Heidelberg, 2000.
- [13] B.D. Tapley, B.E. Schutz, and G.H. Born, *Statistical Orbit Determination*, Elsevier Academic Press, New York, 2004.
- [14] M. Wilkins and K. Alfriend, "Characterizing orbit uncertainty due to atmospheric uncertainty," in *AIAA/AAS Astrodynamics Specialist Conference and Exhibit*, Denver, Colorado, USA, August 2000, American Institute of Aeronautics and Astronautics.
- [15] H. Krag, J. Bendisch, H. Klinkrad, D. Rex, T. Rieger, J. Rosebrock, and T. Schildknecht, "Debris model validation and interpretation of debris measurements using ESA's PROOF tool," *Acta Astronautica*, vol. 48, no. 512, pp. 373–383, 2001.